Exploiting Color Filter Array Sensor NIR Spectral Sensitivity to Improve Color Accuracy: Spectral Reflectance Analysis

Shizhe Shen[1], Roy S. Berns[1], Wonhee Choe[2], SeongDeok Lee[2] and ChangYeong Kim[2]
[1]**Munsell Color Science Laboratory, Center for Imaging Science, Rochester Institute of Technology, Rochester, New York, USA**
[2]**Multimedia Laboratory, Samsung Advanced Institute of Technology, Korea**

Abstract

A visible and near infrared (NIR) spectral reflectance database of commonly imaged objects was developed having minimal spectral redundancy. A spectral analysis was performed on this database to investigate the relationship between NIR and visible spectral reflectance. The correlation between the digital signals of theoretical NIR channels and tristimulus values for the database was analyzed to find the optimal NIR channel such that this channel could be used to improve color accuracy and improve image quality. The closer the NIR channel was located to the visible spectrum, the more optimal was the result. A colorimetric image segmentation algorithm was developed to improve this correlation. The spectral sensitivities of a typical color filter array (CFA) camera were used as a virtual camera model to test the viability of a NIR channel and colorimetric segmentation to improve color accuracy. The simulation results using the database revealed the possibility to exploiting the NIR spectral sensitivities of common CFA cameras as an additional channel for improved color accuracy.

Introduction

Typical color filter array sensors use colored filters that tune the visible spectrum through selective absorption; they also transmit NIR radiation and as a consequence, each color channel has appreciable NIR sensitivity (Figure 13(a)). This sensitivity is usually undesirable and a blue-green colored filter is placed in front of the sensor that absorbs the unwanted NIR radiation and tunes the red channel's spectral sensitivity. (The filter may also perform optical blurring to reduce aliasing.) It is also observed that the sensor quantum efficiency is low. This coupled with the current trend to increase resolution without enlarging the sensor area results in appreciable image noise, particularly under low luminance or high ISO conditions.

Suppose a camera was designed where the NIR sensitivity could be separated from the visible region, either with an additional filter on the CFA (four color), or an additional CFA sensor filtered to only pass long wavelengths. Suppose also that commonly imaged objects had high correlations between the four spectral regions, which we will refer to as RGBI. Under these conditions, the NIR channel could be used to reduce image noise and improve color accuracy under low luminance levels.

NIR imagery has been used widely in night vision devices where complex algorithms were developed to fuse low-light visible and infrared images to achieve "true" or "natural" color images for night vision [1-3]. For common imaging systems,

there are several important issues, such as image noise, image color accuracy, and resolution and spectral frequency response. In the current research, the purpose was to exploit the "undesirable" NIR spectral sensitivities of common imaging systems with a simple camera color model [4] based on the correlation between the spectral reflectance of NIR and visible ranges for commonly imaged objects to improve color accuracy and image noise.

The first step in this research was to perform a spectral analysis on commonly imaged materials to confirm the correlation between NIR and visible range spectral reflectance. A simulation with a virtual camera model was also performed to verify the viability of using an NIR channel to improve color accuracy.

Database Development

A minimum spectral redundancy spectral reflectance database was developed including visible and NIR wavelengths ranging from 400 nm to 1000 nm that consisted of natural and manmade objects. The spectral reflectance data were obtained from the following sources. The ASTER spectral library [5], including the Johns Hopkins University spectral library and the Jet Propulsion Laboratory spectral library, and the United States Geological Survey spectral library [6] were combined (*ASTER*). The second was the spectral database from the Digital Imaging and Remote Sensing Laboratory at Rochester Institute of Technology [7] (*DIRS*). The third was a sampling of the Esser TE221 test chart (*ESSER*). The fourth was current fabrics obtained from a retail fabric store (*Fabric*) and the fifth was color cards of painted samples from a retail paint store (*Paint*). The last three databases were measured using a PhotoResearch PR-715 spectroradiometer. A measurement of sintered Halon was used to convert spectral radiance to spectral reflectance factor. Only the spectral reflectance samples including 400 nm to 1000 nm were selected. Basically, *ASTER* represented the spectral reflectance of soils, rocks, minerals, vegetation, snow, ice and some manmade objects. *DIRS* mainly focused on manmade objects (*e.g.,* car paint, glass, bricks, plastics, cloth, and metals) and some natural objects (*e.g.*, grasses, trees, and woods). *ESSER* represented the spectra of ink on paper with sharp absorptions. *Fabric* included solid-color fabrics, both cotton and nylon. Two substrates were used in order to include different classes of dyes. *Paint* represented the pigments for interior and exterior coatings. The *Fabric* and *Paint* datasets represented current color trends. A sixth database was also created: thirteen measurements of different human skin colors, *Skin*. The idea was to include different kinds of imaged surface colors as much as possible.

For each dataset except for *Skin*, cluster analysis was performed to remove redundant spectra. The purpose was to balance the weighting of different classes of materials in the spectral analysis. The sample numbers of each dataset before and after clustering are show in Table 1.

Table 1. Sample numbers of each dataset

| Database	Before clustering	After clustering
ASTER	765	574
DIRS	383	288
Fabric	80	60
ESSER	112	84
Paint	330	248
Total	1670	1254
Skin	13	

All the databases except for *Skin* were combined to one database. Again, cluster analysis was performed on this combined database to remove redundant spectra between the different databases. The final database contained 941 spectra.

A Savitzky-Golay smoothing filter [8] was used to remove measurement noise in this combined database and the *Skin* database. The spectral reflectances of this minimum spectral redundancy database (*MSR*) and *Skin* are plotted in Figure 1. After interpolation, the spectral reflectance data were defined from 400 nm – 1000 nm with 5 nm intervals. The CIELAB values were calculated using the 1931 2° standard observer and D65, shown in Figure 2.
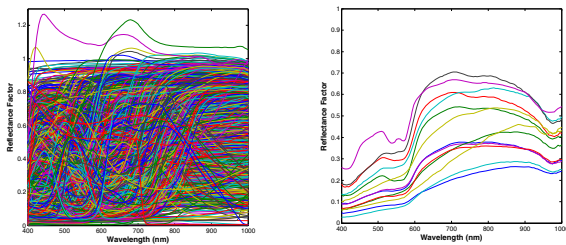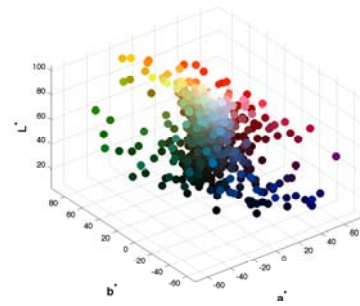

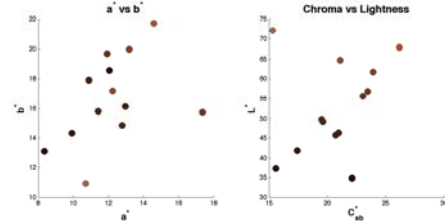(a): MSR database   (b): Skin database

Figure 1. *Spectral reflectance of the MSR (941 samples) and Skin databases (13 samples)*
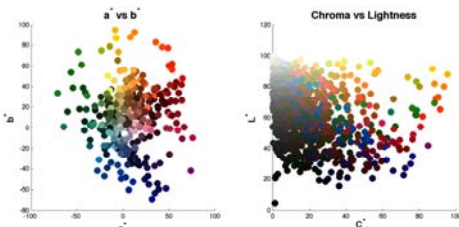
(a): Projection view of the MSR database

(b): Three dimensional view of the MSR database


(c): Projection view of the Skin database

Figure 2. *CIELAB values of the minimum spectral redundancy (MSR) and Skin databases*

Spectral Analysis

The *MSR* and *Skin* databases were analyzed separately realizing the unique position of skin color when imaging. The analysis included principal component analysis (PCA) [9] and Pearson correlation coefficients. The results were plotted in Figures 3 and 4, respectively.
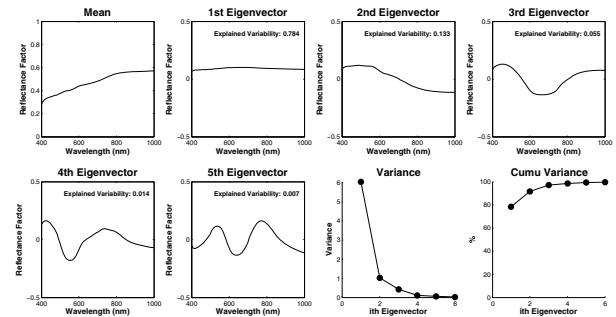
(a): MSR database
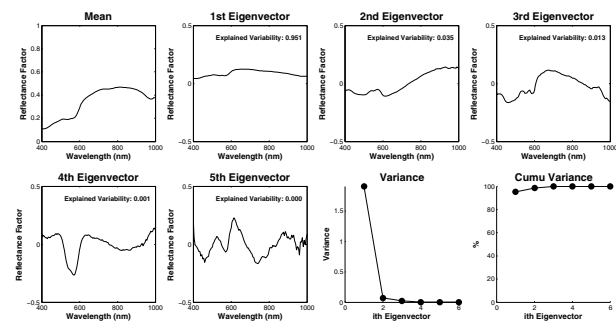
(b):Skin database

Figure 3. *PCA analysis results of the MSR and Skin databases*

For the *MSR* database, the first eigenvector was flat indicating that many of these samples were composed of spectrally non-selective colorants such as carbon-containing pigments. Four to five eigenvectors were required to describe the variance with sufficient accuracy. The mean reflectance in Figure 3 (b) reveals the high spectral reflectance of skin in the NIR range, which suggested the potential applications of NIR channels in improving image quality of portraiture. The second and the third eigenvectors show the hemoglobin absorptions [10, 11]. Typically, three eigenvectors are sufficient to describe the spectral variability of skin spectra.

Pearson correlation coefficients were computed for the spectral data between each pair of wavelengths for each database. The results are shown in Figure 4. The correlation between NIR and visible spectra was weak for the *MSR* database. The closer the NIR wavelength was to the visible region, the better the correlation. The correlation coefficients for *Skin* revealed high correlation between NIR and visible wavelengths.
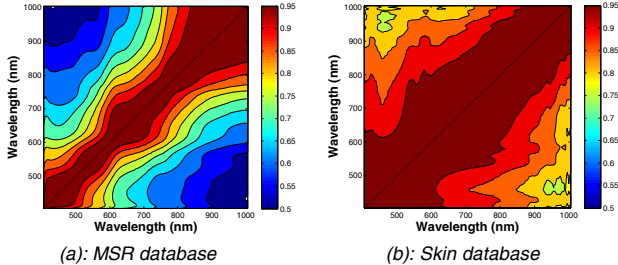

(a): MSR database   (b): Skin database

Figure 4. *Pearson correlation coefficients for the MSR and the Skin databases*

Correlations Between NIR Channels and Tristimulus Values

A camera model was defined where long-pass filters between 640 nm and 1000 nm in 20 nm increments simulated a set of NIR channels, plotted in Figure 5. The starting wavelength of 640 nm was selected because a camera that is designed for color accuracy usually has peak sensitivities below 640 nm. The virtual digital signals of samples of both databases were calculated using this camera model with assumed equal-energy illumination. In addition, CIE tristimulus values were calculated for each spectrum for illuminant D65 and the 1931 2° standard observer. The relationship between virtual digital counts and the tristimulus values is shown in Figures 6 and 7 for *MSR* and *Skin*, respectively. In Figures 6 and 7, only the digital counts of two channels with cut-off wavelengths of 640 nm and 1000 nm are plotted. Generally, the signals from channels with cut-off wavelength closer to the visible range had better correlation with tristimulus values than these far away from the visible range. For the Skin database, the correlation between the NIR signals and the tristimulus values was quite good.

Linear least squares regression was performed between the independent variables, the signals of each channel, and dependent variables, the tristimulus values, and a correlation coefficient (r^2) was calculated to indicate the extent of scatter. A correlation coefficient approaching unity indicates minimal

scatter and that the dependent variables could be well predicted from the independent variables. The r^2 for each tristimulus value as a function of wavelength is plotted in Figure 8. As anticipated, the correlation increased with the decrease of cut-off wavelength, since shorter wavelengths are closer to the visible range. Tristimulus values Z had the lowest correlation because the corresponding color matching function is located in the short visible wavelength region, furthest from the NIR.
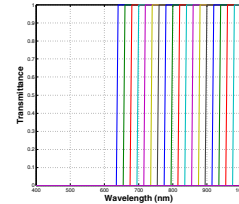

Figure 5. *Transmittance of the filters for the camera model*

(a): 640nm cut-off filter

(b): 1000nm cut-off filter
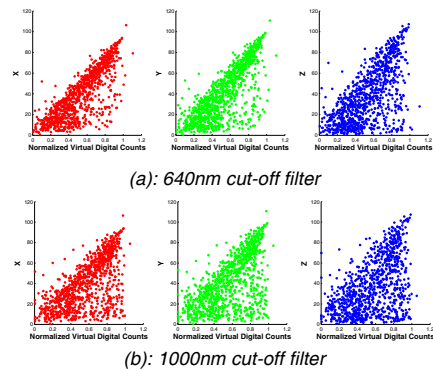
Figure 6. *Camera signals vs. X, Y, Z for the MSR database*

(a): 640nm cut-off filter

(b): 1000nm cut-off filter
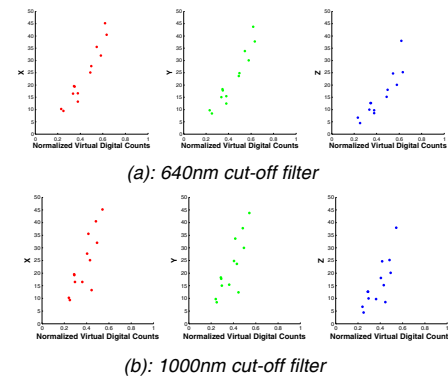
Figure 7. *Camera signals vs. X, Y, Z for the Skin database*

(a): MSR database   (b): Skin database

Figure 8. *r^2 between the signals from the cut-off wavelength channels and each listed tristimulus values based on linear regression*

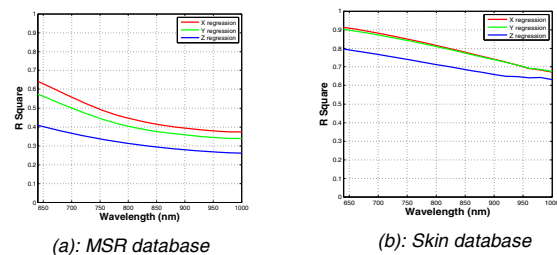In addition, the average color differences between the predicted tristimulus values from the regression and the actual tristimulus values for all 941 samples were calculated for the *MSR* and the *Skin* databases and shown in Figure 9. The large average color differences for *MSR* represented the weak global linear relationship between the virtual signals from NIR channels and the colorimetric coordinates.
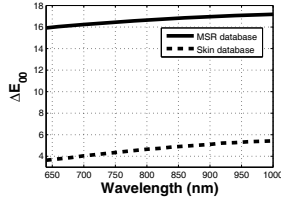

Figure 9. *Average color difference evaluating the performance of the linear regression color prediction*

Step-wise multiple-linear regression was performed between the digital counts of all NIR channels as independent variables and the tristimulus values as dependent variables. The results are shown in Table 2. In Table 2, the signals from these channels that had p-values smaller than 0.05 had statistically significant effects on the regression results if these channels were removed from the list of independent variables. β_i represented the regression coefficients of each channel after removing these insignificant channels. The absolute values of the t-statistics provided the significance of different channels in the regression. The similar trend to that described above was illustrated in Table 2: channels closer to visible range had a larger effect on the regression, indicating higher correlation between these signals and the tristimulus values. The first six channels had the largest effect on the regression.

Colorimetric Image Segmentation to Improve Correlation

The above analysis revealed that global correlation between NIR spectra and visible spectra (or the signals from NIR channels and the colorimetric values) of commonly imaged objects was weak, which suggested that segmentation in a color space might achieve higher local correlations. More sub-spaces will achieve better local correlation in segmentation and the maximum number of sub-spaces will be determined by the computational capability of the imaging system. (Image quality issues related to segmentation are beyond the scope of this research.) Here, as a proof of concept, the segmentation was optimized by evaluating the CIELAB parameters of L^*, C^*_{ab} and h_{ab}, independently. Namely, the CIELAB space was first segmented by: one constant L^* plane, one constant C^*_{ab} cylindrical surface, and four constant h_{ab} planes, separately. These four planes are parallel or perpendicular to each other and divided the space into four equal subspaces. These constant L^*, C^*_{ab} and h_{ab} values of these surfaces were designated as "gate values." These gate values were optimized through the multi-linear regression between the digital counts of the first six channels (640nm – 740nm in 20nm increments) of the camera model and the tristimulus values for the *MSR* database. The first six channels were selected based on the step-wise multi-linear regression results listed in Table 2, in which the first six channels represented significant influence on the regression

performance. The results of optimization on gate values are shown in Figure 10, in which the residual error was plotted as a function of gate value.
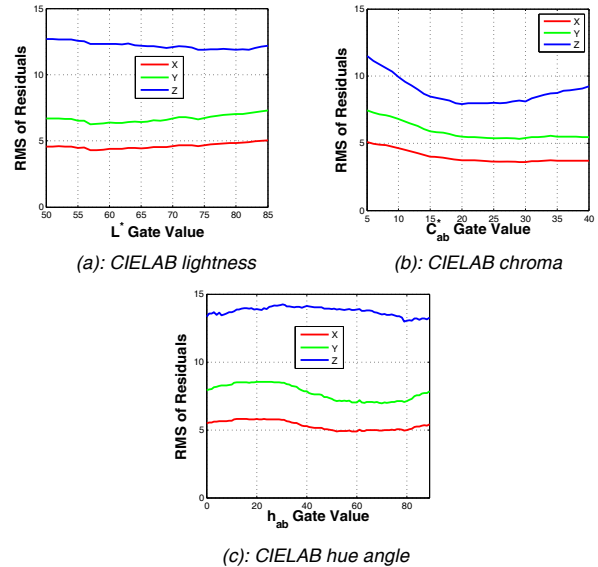

(a): CIELAB lightness   *(b): CIELAB chroma*

(c): CIELAB hue angle

Figure 10. *Residual error as a function of CIELAB lightness, chroma and hue angles for tristimulus values*

Without segmentation, the RMS residuals of regression on X, Y and Z for the *MSR* database were 6.72, 9.92, and 17.26, respectively. After segmentation, the regression performance improved. In Figure 10(b) for chroma, segmentation had a noted improvement when selecting the optimal gate values. In Figure 10(a) for lightness and Figure 10(c) for hue angles, different gate values did not have an impact on performance. It was decided to segment CIELAB space with the optimal gate values $L^* = 57$, $C^*_{ab} = 27$ and $h_{ab} = 80°$, 170°, 260° and 350°. This resulted in 16 sub-spaces. The segmentation results for the *MSR* database are shown in Table 3. It was interesting to find that there were no high lightness, high chroma blues and few high lightness, high chroma greens in the *MSR* database. The largest group was high lightness, low chroma yellow colors that represented the scenes of soils and metal oxides.

Table 3. Segmentation results for the *MSR* database

Group	No.	L*	C*	h*
1	69	Dark	Low	Quadrant 1 (Yellowish)
2	26	Dark	Low	Quadrant 2 (Greenish)
3	21	Dark	Low	Quadrant 3 (Bluish)
4	69	Dark	Low	Quadrant 4 (Reddish)
5	18	Dark	High	Quadrant 1 (Yellowish)
6	11	Dark	High	Quadrant 2 (Greenish)
7	31	Dark	High	Quadrant 3 (Bluish)
8	75	Dark	High	Quadrant 4 (Reddish)
9	324	Light	Low	Quadrant 1 (Yellowish)
10	53	Light	Low	Quadrant 2 (Greenish)
11	49	Light	Low	Quadrant 3 (Bluish)
12	100	Light	Low	Quadrant 4 (Reddish)
13	46	Light	High	Quadrant 1 (Yellowish)
14	5	Light	High	Quadrant 2 (Greenish)
15	0	Light	High	Quadrant 3 (Bluish)
16	44	Light	High	Quadrant 4 (Reddish)
Sum	941			

The spectral reflectances of samples in each group are shown in Figure 11. For some groups, the spectra were similar, such as for groups 6 and 8 while for the other groups, there was quite a bit of variability.
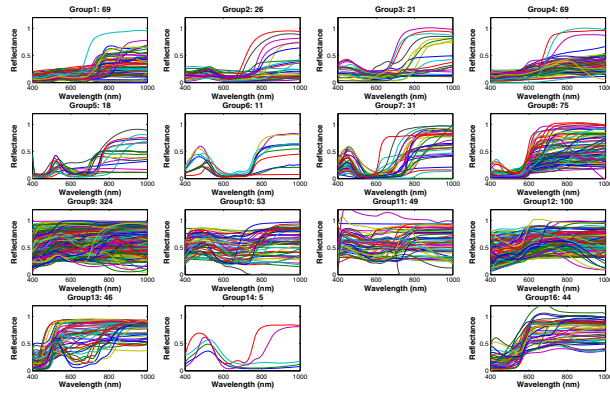

Figure 11. Spectral reflectance divided into CIELAB subgroups

Linear regression was performed between the digital counts of each cut-off channel and the tristimulus values for each group, separately. The average color difference for all 941 samples was 8.7 ΔE_{00}, which was much smaller than the average color difference around 17 ΔE_{00} plotted in Figure 9. This supported the viability of image segmentation by color as an aid to using NIR signals in color processing.

Effect of Using an NIR channel and Image Segmentation on Color Accuracy

The effect of using an NIR channel and image segmentation on color accuracy was simulated as the workflow in Figure 12. The digital counts of RGB channels were used to roughly estimate CIELAB values and these CIELAB values were employed for segmentation. The segmentation can also be done in other spaces, such as RGB channels and XYZ tristimulus values. Here, the workflow was only one example of the implementation.
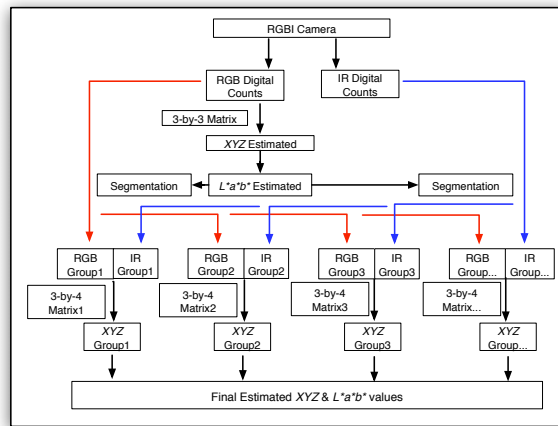

Figure 12. Implementation flowchart

The spectral sensitivities of a Sinar™ 54H (as plotted in Figure 13 (a)), an RGB CFA digital camera, were used to represent a typical CFA digital camera. A blue-green filter was added to the system, resulting in the RGB sensitivities plotted in Figure 13 (b). In addition, the NIR channel was assumed to have the sensitivities of the red channel in Figure 13 (a) with a 640 nm cut-off filter. Because of the larger quantum efficiency for the red channel, the NIR channel had sensitivity even higher than the green channel.
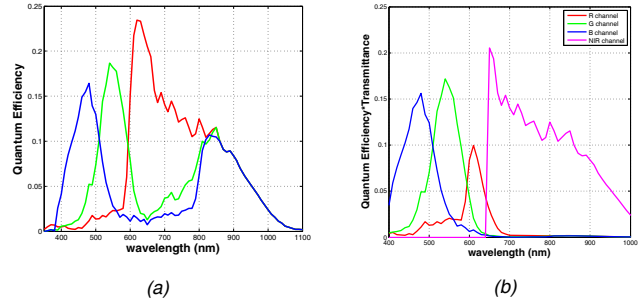

(a)   *(b)*

Figure 13. Spectral sensitivities of the virtual camera model with R, G, B and NIR channels

The virtual digital counts of 941 spectra of the MSR database were calculated assuming equal-energy illumination. Nonlinear optimization was used to build the colorimetric-based (3x3) or (3x4) matrices [4] to convert the camera signals (either without or with the NIR channel) to tristimulus values for D65 and 1931 2° standard observer. The optimization minimized the average CIEDE2000 color difference. Three different methods were used for comparative purposes: using three channels (RGB) without segmentation, using four channels (RGBI) without segmentation, and using four channels (RGBI) with segmentation. The histograms of the prediction results are shown in Figure 14.

(a): RGB w/o Segmentation   *(b):RGBI w/o segmentation*
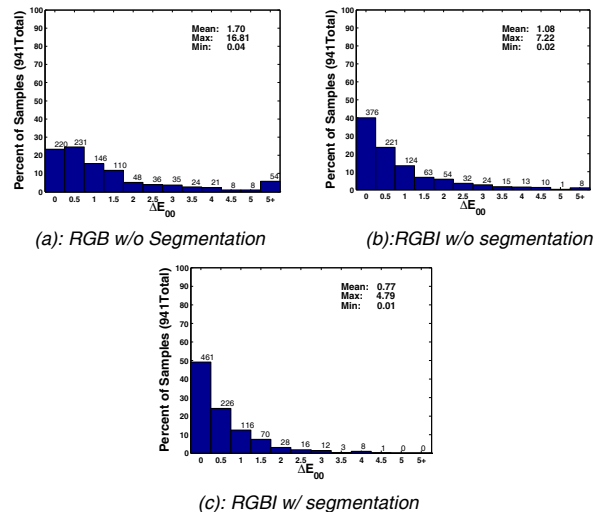

(c): RGBI w/ segmentation

Figure 14. Color difference histograms illustrating the effect of NIR channels and using segmentation on color accuracy

The average CIEDE2000 of 1.7 is typical for a CFA three-channel camera with a well-selected blue-green filter [12]. The maximum error of this three-channel camera was 16.8 ΔE_{00} and

a large number of samples had color differences greater than 5 ΔE_{00}. The addition of the NIR channel had a marked effect on performance. The average color difference decreased from 1.7 to 1.1 ΔE_{00}. The maximum color difference was greatly reduced from 16.8 to 7.2 ΔE_{00}. With segmentation, the performance was further improved with average and maximum errors of 0.8 and 4.8 ΔE_{00}, respectively. This result proved the viability of a NIR channel and using segmentation to improve the color accuracy of camera systems.

Conclusions

This research explored the viability of exploiting the NIR spectral sensitivities of CFA cameras as an additional channel to improve color accuracy based on the analysis of a database of commonly imaged objects with minimal spectral redundancy. The theoretical simulation results revealed that with proper implementation, the NIR channel improved color accuracy appreciably, particularly by reducing the maximum errors. In our experience, observers are very sensitive to outliers when evaluating color image quality.

References

[1] A. M. Waxman, et al. Solid-state color night vision: fusion of low-light visible and thermal infrared imagery, *MIT Lincoln Laboratory Journal* **11,** 41-60 (1998)

[2] V. Tsagaris and V. Anastassopoulos, Fusion of visible and infrared imagery for night color vision, *Displays* **26,** 191-196 (2005)

[3] E. P. Bennett, J. L. Mason and L. McMillan, Multispectral bilateral video fusion, *IEEE Trans. Image Processing* **16,** 1185-1194 (2007)

[4] R. S. Berns, *Billmeyer and Saltzman's Principles of Color Technology*, 3rd edition, John Wiley & Sons. Inc., 2000

[5] ASTER spectral library, http://speclib.jpl.nasa.gov/

[6] US Geological Survey spectral library, http://speclab.cr.usgs.gov/spectral-lib.html

[7] Digital Imaging and Remote Sensing Laboratory, Center for Imaging Science, Rochester Institute of Technology. http://dirs.cis.rit.edu/

[8] S. J. Orfanidis, *Introduction to Signal Processing*, Prentice-Hall, 1996

[9] D. Y. Tzeng and R. S. Berns, A review of principal component analysis and its applications to color technology, *Color Res. Appl.* **30,** 84-98 (2005)

[10] E. Angelopoulou, Understanding the color of human skin, *SPIE Proc.* **4299,** 243-251 (2001)

[11] E. Angelopoulou, R. Molana and K. Daniilidis, Multispectral skin color modeling, *IEEE Conference on Computer Vision and Pattern Recognition,* **2,** II-635-II-642 (2001)

[12] Y. Zhao, L. A. Taplin, M. Nezamabadi and R. S. Berns, Methods of spectral reflectance reconstruction for a Sinarback 54 digital camera, Technical Report. Munsell Color Science Laboratory, Center for Imaging Science, Rochester Institute of Technology (2004)

Author Biography

Shizhe Shen received his BS (2002) and MS (2005) in optical engineering from Zhejiang University, China. He will also receive MS in color science from Munsell Color Science Laboratory at RIT, Rochester, New York (2008). His work has also focused on color difference equation and uniform color space modeling.

Table 2. Step-wise multi-linear regression results

Channels (Cut-off wavelength, nm)	With X			With Y			With Z		
	β_i	t-stats	p-value	β_i	t-stats	p-value	β_i	t-stats	p-value
640	9886.6	19.86	0.00	12695.7	18.61	0.00	14358.8	11.12	0.00
660	-24408.9	-16.06	0.00	-30921.4	-16.07	0.00	-39745.4	-9.67	0.00
680	25315.4	11.47	0.00	29383.7	13.41	0.00	50058.0	7.66	0.00
700	-16335.5	-7.17	0.00	-14915.6	-11.05	0.00	-42938.3	-5.67	0.00
720	6996.1	4.56	0.00	3891.3	9.73	0.00	26773.6	4.33	0.00
740	-1372.9	-2.93	0.00	0.0	-1.76	0.08	-11062.6	-3.39	0.00
760	0.0	1.03	0.30	0.0	-1.47	0.14	2732.4	3.01	0.00
780	0.0	0.06	0.96	0.0	-1.05	0.30	0.0	-1.12	0.26
800	0.0	-0.31	0.76	0.0	-0.28	0.78	0.0	-1.07	0.29
820	0.0	-0.51	0.61	0.0	0.34	0.73	0.0	-1.04	0.30
840	0.0	-0.69	0.49	0.0	0.76	0.45	0.0	-1.02	0.31
860	0.0	-0.93	0.35	0.0	1.00	0.32	0.0	-1.03	0.30
880	0.0	-1.15	0.25	0.0	1.17	0.24	0.0	-1.07	0.29
900	0.0	-1.18	0.24	0.0	1.34	0.18	0.0	-1.15	0.25
920	814.0	3.85	0.00	0.0	1.34	0.18	0.0	-1.41	0.16
940	-1371.5	-3.70	0.00	-44.5	-4.68	0.00	0.0	-1.89	0.06
960	563.4	3.27	0.00	0.0	0.11	0.92	0.0	-1.84	0.07
980	0.0	-0.71	0.48	0.0	0.04	0.97	0.0	-1.62	0.10
1000	0.0	-0.84	0.40	0.0	-0.21	0.83	-96.9	-5.58	0.00